

Article

Double Perovskite Mn⁴⁺-Doped La₂CaSnO₆/La₂MgSnO₆ Phosphor for Near-Ultraviolet Light Excited W-LEDs and Plant Growth

Zheng Lu ^{1,2}, Dashuai Sun ^{2,*}, Zeyu Lyu ², Sida Shen ², Jianhui Wang ^{1,2}, Hanwei Zhao ^{1,2}, Lixuan Wang ^{1,2} and Hongpeng You ^{1,2,3,*} 

¹ School of Rare Earths, University of Science and Technology of China, Hefei 230026, China

² Ganjiang Innovation Academy, Chinese Academy of Sciences, Ganzhou 341000, China

³ State Key Laboratory of Rare Earth Resource Utilization, Changchun Institute of Applied Chemistry, Chinese Academy of Sciences, Changchun 130022, China

* Correspondence: dssun@gia.cas.cn (D.S.); hpyou@ciac.ac.cn (H.Y.); Tel.: +86-431-8526-2798 (H.Y.)

Abstract: Non-rare earth doped oxide phosphors with far-red emission have become one of the hot spots of current research due to their low price and excellent physicochemical stability as the red component in white light-emitting diodes (W-LEDs) and plant growth. Herein, we report novel Mn⁴⁺-doped La₂CaSnO₆ and La₂MgSnO₆ phosphors by high-temperature solid-phase synthesis and analyzed their crystal structures by XRD and Rietveld refinement. Their excitation spectra consist of two distinct excitation bands with the dominant excitation range from 250 to 450 nm, indicating that they possess strong absorption of near-ultraviolet light. Their emission is located around 693 and 708 nm, respectively, and can be absorbed by the photosensitive pigments Pr and Pfr, proving their great potential for plant growth. Finally, the prepared samples were coated with 365 nm UV chips to fabricate far-red LEDs and W-LEDs with low correlation color temperature (CCT = 4958 K/5275 K) and high color rendering index (R_a = 96.4/96.6). Our results indicate that La₂CaSnO₆:Mn⁴⁺ and La₂MgSnO₆:Mn⁴⁺ red phosphors could be used as candidate materials for W-LED lighting and plant growth.

Keywords: red phosphor; luminescent properties; W-LEDs; plant growth



Citation: Lu, Z.; Sun, D.; Lyu, Z.; Shen, S.; Wang, J.; Zhao, H.; Wang, L.; You, H. Double Perovskite Mn⁴⁺-Doped La₂CaSnO₆/La₂MgSnO₆ Phosphor for Near-Ultraviolet Light Excited W-LEDs and Plant Growth. *Molecules* **2022**, *27*, 7697. <https://doi.org/10.3390/molecules27227697>

Academic Editors: Liang Zhou, Xue-Li Hao and Weiqiang Liu

Received: 9 October 2022

Accepted: 5 November 2022

Published: 9 November 2022

Publisher's Note: MDPI stays neutral with regard to jurisdictional claims in published maps and institutional affiliations.



Copyright: © 2022 by the authors. Licensee MDPI, Basel, Switzerland. This article is an open access article distributed under the terms and conditions of the Creative Commons Attribution (CC BY) license (<https://creativecommons.org/licenses/by/4.0/>).

1. Introduction

As the latest generation of lighting sources, light-emitting diodes (LEDs) have been successfully used in many fields and have contributed to the development of these fields, especially in agriculture, because of their outstanding advantages such as high efficiency, environmental protection, and energy reduction [1–5]. As the most basic source of energy for the survival and reproduction of all living things on earth, the role played by light in the growth of plants is self-evident [6–10]. However, not all wavelengths of light are absorbed by the pigments in plants, with visible light (380–720 nm) and near-infrared light (720–800 nm) being the absorption ranges [11–14]. In contrast, near-ultraviolet (n-UV) light (290–380 nm) plays a negligible role in the plant growth process. In order to enable plants to utilize the energy of n-UV light, there is an urgent need for a light-converting phosphors that can convert n-UV light to visible or near-infrared light. Therefore, it is crucial to find phosphors that can be excited by n-UV light.

In recent years, Mn⁴⁺ ion has attracted much attention due to its abundant reserves and low prices. It is well known that Mn⁴⁺ ion is a good non-rare earth activator, which usually occupies an octahedral coordination environment in the lattice and has outstanding optical properties, including a broad absorption band covering the UV to visible region and characteristic red luminescence in the wavelength range from red to near-infrared light [15–18]. Intriguingly, the luminescence of the Mn⁴⁺ ions is right within the absorption range of the photosensitive pigments Pr (red light-absorbing form) and Pfr (far-red light-absorbing form) in plants. The photosensitive pigment is one of the most important photoreceptors

for plant photomorphogenesis, and its role is indispensable for the developmental process of plants. It is not only involved in regulating plant growth and development, but also in responding to biotic and abiotic stresses. The absence of photosensitive pigments leads to altered plant resistance to biotic stresses such as pathogenic bacteria and pests, as well as abiotic stresses such as low temperature, high temperature, drought, and salt, while the resistance of plants to these adverse stresses can be improved by changing the light quality (e.g., adjusting the red far-red light ratio). Therefore, Mn^{4+} -doped phosphors can be applied in plant growth.

There have been many reports on Mn^{4+} -doped phosphors [5]. However, there have been no reports on the use of La_2CaSnO_6 and La_2MgSnO_6 crystals for the synthesis of red or deep-red luminescent phosphors. In this work, we report a series of novel red-emitting double perovskite structures of $La_2CaSnO_6:Mn^{4+}$ (LCSO: Mn^{4+}) and $La_2MgSnO_6:Mn^{4+}$ (LMSO: Mn^{4+}) phosphors obtained by high-temperature solid-phase reactions. The phase purity and crystal structures were characterized by XRD and Rietveld refinement. The luminescence properties of the prepared phosphors were investigated, including photoluminescence properties, temperature-dependent luminescence properties, quantum efficiency, and fluorescence lifetime. Furthermore, by combining with n-UV LED chips and commercial phosphors, both W-LEDs can produce white light with high CRI and low CCT. This paper demonstrates the potential of $La_2CaSnO_6:Mn^{4+}$ and $La_2MgSnO_6:Mn^{4+}$ phosphors for applications in W-LEDs and plant growth.

2. Results and Discussion

2.1. Structural Properties

Figure 1a,b show the XRD patterns of LCSO: xMn^{4+} ($x = 0.002, 0.004, 0.006, 0.008, 0.010$) and LMSO: yMn^{4+} ($y = 0.002, 0.004, 0.006, 0.008, 0.010$) samples. Obviously, the diffraction peaks of the Mn^{4+} -doped samples with different concentrations match with those of the standard data and no impurity peaks are found, indicating that all the Mn^{4+} ions are dissolved in the main lattice. We tested the X-ray photoelectron spectra (XPS) of LCSO:0.002 Mn^{4+} and LMSO:0.002 Mn^{4+} , and the results are shown in Figure 1c,d. The signals of La, Sn, Ca, Mg, and O elements were clearly detected. The XPS spectra of Mn 2p are shown in Figure 1e,f, and it can be observed that the binding energy peak of Mn 2P_{1/2} of both are located near 654 eV, and the binding energy peak of Mn 2p_{3/2} of both is located near 642 eV, which proves that the oxidation state of Mn is +4.

To further explore the crystal structures of LCSO and LMSO, the crystal structure data of Ca_2LaTaO_6 (ICSD 251945) and $La(Mg_{0.5}Sn_{0.5})O_3$ (ICSD 156359) were used as starting base models for LCSO:0.004 Mn^{4+} and LMSO:0.010 Mn^{4+} Rietveld structure refinement, and the results are shown in Figure 2a,b [19,20]. The refinement results showed that LCSO:0.004 Mn^{4+} and LMSO:0.010 Mn^{4+} were pure phases. The detailed crystallographic data are shown in Table 1.

Table 1. Main crystallographic parameters of LCSO:0.004 Mn^{4+} and LMSO:0.010 Mn^{4+} .

Compound	$La_2CaSnO_6:0.004Mn^{4+}$	$La_2MgSnO_6:0.010Mn^{4+}$
Space group	$P2_1/n$	$P2_1/n$
a, Å	5.74019	5.63776
b, Å	5.95969	5.72036
c, Å	8.25804	8.02015
$\alpha = \gamma$	90°	90°
β	89.99°	90.06°
V	282.506	258.650
Crystal system	Monoclinic	Monoclinic
Z	2	2
R_{wp} , %	6.08	8.26
R_p , %	4.83	5.33
χ^2	1.008	2.173

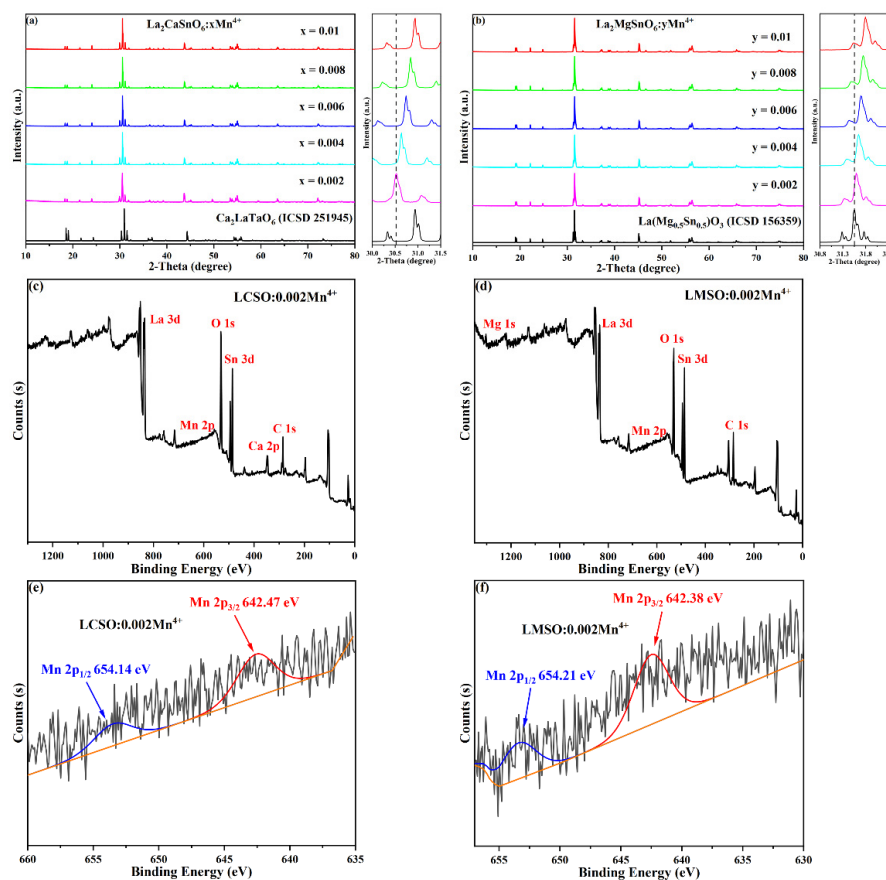


Figure 1. (a) XRD patterns of $\text{LCSO}:x\text{Mn}^{4+}$ ($x = 0.002, 0.004, 0.006, 0.008,$ and 0.010). (b) XRD patterns of $\text{LMSO}:y\text{Mn}^{4+}$ ($y = 0.002, 0.004, 0.006, 0.008,$ and 0.010). (c) XPS spectrum of the $\text{LCSO}:0.002\text{Mn}^{4+}$. (d) XPS spectrum of the $\text{LMSO}:0.002\text{Mn}^{4+}$. (e) Mn 2p XPS spectrum of the $\text{LCSO}:0.002\text{Mn}^{4+}$. (f) Mn 2p XPS spectrum of the $\text{LMSO}:0.002\text{Mn}^{4+}$.

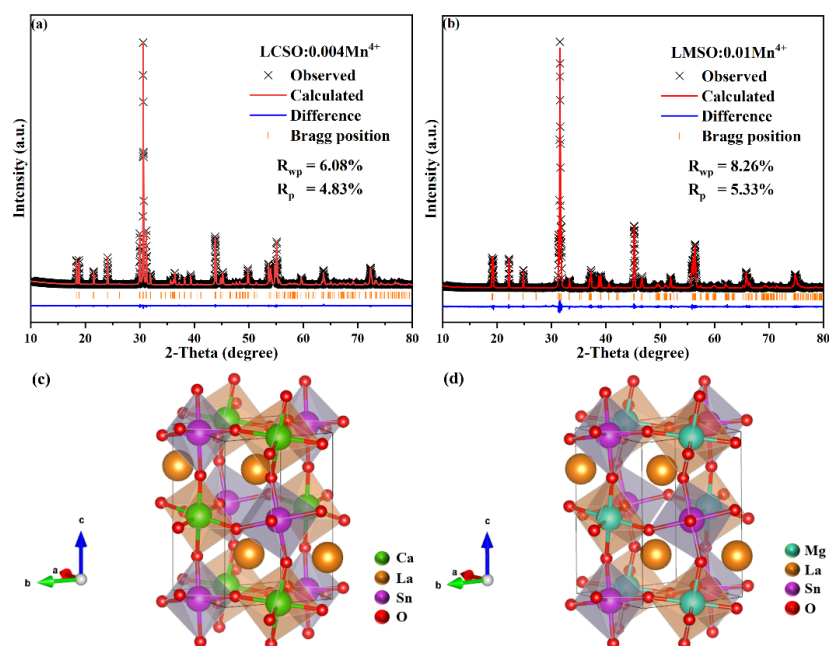


Figure 2. (a) Rietveld refinements of $\text{LCSO}:0.004\text{Mn}^{4+}$. (b) Rietveld refinements of $\text{LMSO}:0.01\text{Mn}^{4+}$. (c) Crystal structure of $\text{LCSO}:0.004\text{Mn}^{4+}$. (d) Crystal structure of $\text{LMSO}:0.01\text{Mn}^{4+}$.

The crystal structures of LCSO and LMSO were obtained by refining the crystallization results in the $P2_1/n$ space group, and the results are shown in Figure 2c,d. $\text{La}_2\text{CaSnO}_6$ and $\text{La}_2\text{MgSnO}_6$ have the structural general formula $\text{A}_2\text{BB}'\text{O}_6$, where the A, B, and B' sites are occupied by La, Ca/Mg, and Sn atoms, respectively. The B site binds to O^{2-} to form CaO_6 , MgO_6 , and SnO_6 octahedra. The $\text{CaO}_6/\text{MgO}_6$ octahedron and the SnO_6 octahedron have a common oxygen atom at the apex of both, and these two octahedra are staggered to form a long-range-ordered structural layer. The A site occupies the gap between the $[\text{BO}_6]$ octahedra and coordinates with twelve O^{2-} . In the LCSO and LMSO crystal structures, there are three cations available for Mn^{4+} occupation. Considering the three aspects of ionic radius, valence state and coordination number, among the four ions La^{3+} ($r = 1.1 \text{ \AA}$, CN = 7), Ca^{2+} ($r = 1 \text{ \AA}$, CN = 6), Mg^{2+} ($r = 0.72 \text{ \AA}$, CN = 6), and Sn^{4+} ($r = 0.69 \text{ \AA}$, CN = 6), the Sn^{4+} site is considered the most suitable Mn^{4+} ($r = 0.53 \text{ \AA}$, CN = 6) doping site.

2.2. Photoluminescence Properties

The excitation and emission spectra of $\text{La}_2\text{CaSnO}_6:0.002\text{Mn}^{4+}$ and $\text{La}_2\text{MgSnO}_6:0.002\text{Mn}^{4+}$ at room temperature are shown in Figure 3a,b. The photoluminescence excitation (PLE) spectra monitored at 693 and 708 nm show two distinct excitation bands with the dominant excitation range from 250 to 450 nm and the weak excitation range from 450 to 600 nm, due to the $\text{Mn}^{4+}-\text{O}^{2-}$ charge transition band (CTB), ${}^4\text{A}_{2g} \rightarrow {}^4\text{T}_{1g}$, ${}^4\text{A}_{2g} \rightarrow {}^2\text{T}_{2g}$, and ${}^4\text{A}_{2g} \rightarrow {}^4\text{T}_{2g}$ transitions [21,22]. As shown in Figure 3c,d, the Gaussian fit analysis of the energy-based PLE spectra of these two samples shows that the above four effects correspond roughly to $28,508 \text{ cm}^{-1}$, $25,943 \text{ cm}^{-1}$, $24,514 \text{ cm}^{-1}$, and $18,768 \text{ cm}^{-1}$ for $\text{LCSO}:0.002\text{Mn}^{4+}$, and $28,816 \text{ cm}^{-1}$, $26,381 \text{ cm}^{-1}$, $25,458 \text{ cm}^{-1}$, and $19,342 \text{ cm}^{-1}$ for $\text{LMSO}:0.002\text{Mn}^{4+}$. Both exhibit intense red emission under 365 nm UV excitation due to the spin-prohibited ${}^2\text{E}_g \rightarrow {}^4\text{A}_{2g}$ leap of the Mn^{4+} ions in the octahedral environment, with the peak emission near 693 nm for $\text{LCSO}:0.002\text{Mn}^{4+}$ and around 708 nm for $\text{LMSO}:0.002\text{Mn}^{4+}$, which can be absorbed by the photosensitive pigments Pr and Pfr [23]. These results prove that both phosphors are well suited for n-UV chips and are potential red-emitting phosphors, as well as able to be applied in plant growth. In addition, the emission spectra of both were found to show several sharp peaks. These peaks consist of the anti-Stokes emission, the zero-phonon line (ZPL) of the ${}^2\text{E}_g \rightarrow {}^4\text{A}_{2g}$ transition, and the Stokes emission [10,16]. Figure 3e,f show the emission spectra of $\text{LCSO}:0.002\text{Mn}^{4+}$ and $\text{LMSO}:0.002\text{Mn}^{4+}$ at 7 K. The ZPL of the ${}^2\text{E}_g \rightarrow {}^4\text{A}_{2g}$ transition was found to occur at 678 nm ($14,749 \text{ cm}^{-1}$) and 692 nm ($14,451 \text{ cm}^{-1}$), respectively.

The photoluminescence (PL) spectra of a series of different concentrations of $\text{LCSO}:x\text{Mn}^{4+}$ ($x = 0.001-0.010$) and $\text{LMSO}:y\text{Mn}^{4+}$ ($x = 0.001-0.010$) were tested as shown in Figure 4a,b. All samples with different doping concentrations show no absence and shift of emission peaks, only changes in emission intensity. From Figure 4c,d, it can be seen that $\text{LCSO}:x\text{Mn}^{4+}$ ($x = 0.001-0.010$) and $\text{LMSO}:y\text{Mn}^{4+}$ ($y = 0.001-0.010$) have the same trend, and the emission intensity increases with the increase in doping concentration from 0.001 to 0.002 and decreases with the increase from 0.002 to 0.01, and the optimal doping concentration for both was determined as 0.002. When the doping concentration exceeds 0.002, the emission intensity starts to decrease, and the concentration quenching appears and becomes more severe with the increase in the Mn^{4+} content. The concentration quenching includes two mechanisms: exchange interaction and multistage-multistage interaction. To investigate which mechanism causes the concentration quenching, we calculated the critical distance R_c by the following equation [24,25]:

$$R_c \approx 2 \left(\frac{3V}{4\pi x_c N} \right)^{\frac{1}{3}} \quad (1)$$

where V is the volume of the unit cell, x_c is the critical concentration, and N represents the number of sites that the Mn^{4+} ions can occupy per unit cell. For the LCSO host, $V = 282.506 \text{ \AA}^3$, $N = 2$, and $x_c = 0.002$; the critical distance R_c is calculated to be 51.29 \AA . For the LMSO host, $V = 258.650 \text{ \AA}^3$, $N = 2$, and $x_c = 0.002$; the critical distance R_c is calculated

to be 49.81 Å. Because the exchange interaction is effective only when the distance between activators is shorter than 5 Å, the concentration quenching mechanism of the Mn⁴⁺ ions in phosphors is dominated by multipole–multipole interactions. According to Van Uiter’s report, the emission intensity (I) per activator ion follows the equation [26]:

$$\frac{I}{x} = K \left[1 + \beta(x)^{\frac{\theta}{3}} \right]^{-1} \quad (2)$$

where x is the activator concentration, I/x is the emission intensity per activator concentration, K and β are the constants for the same excitation conditions, and θ = 6, 8, and 10 represent the dipole–dipole(d-d), dipole–quadrupole(d-q), and quadrupole–quadrupole(q-q) interactions. Figure 5a,b show a plot of log(I/x) versus log(x), with −θ/3 being the slope. For LCSO, a slope of −1.62 gives a θ of 4.86, which is closer to 6. For LMSO, a slope of −1.93 gives a θ of 5.79, again close to 6. These results suggest that dipole–dipole interactions dominate the concentration quenching mechanism of Mn⁴⁺ emission in LCSO and LMSO.

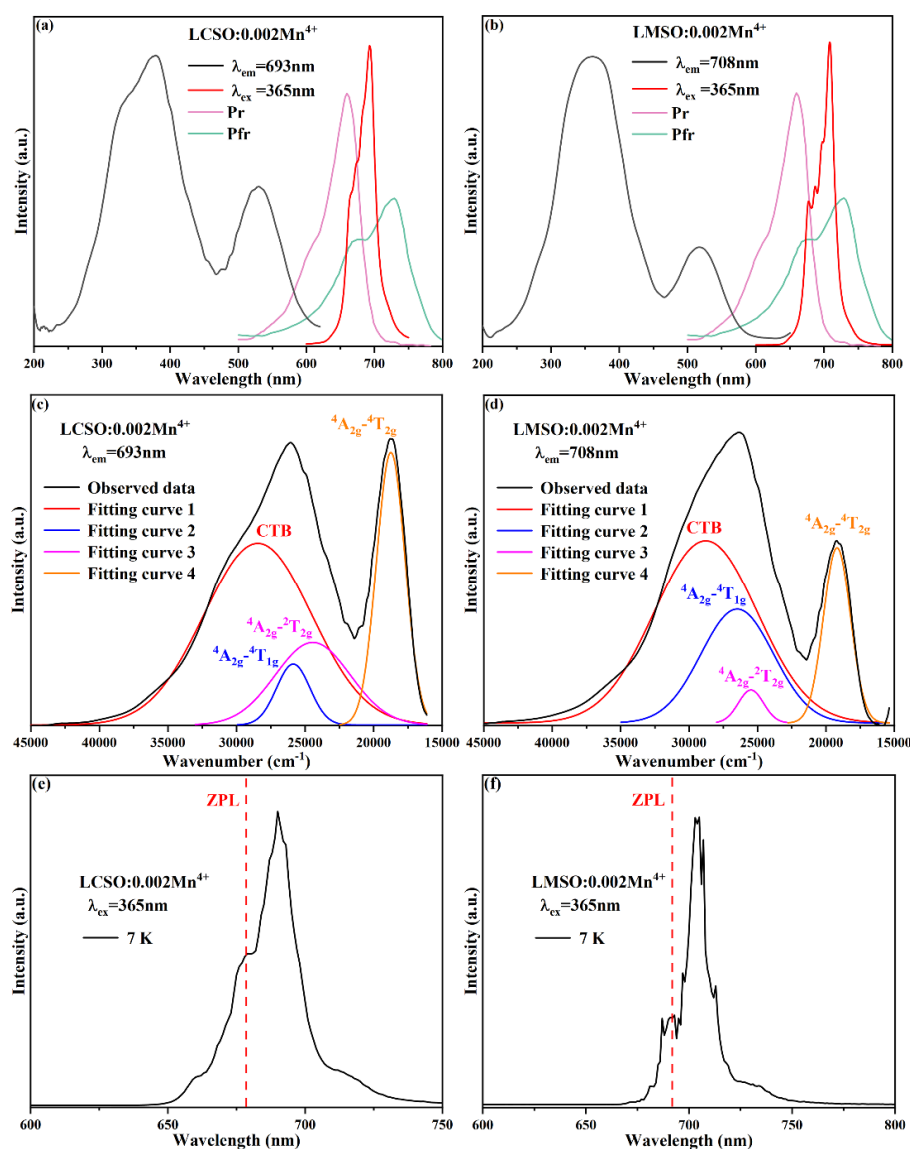


Figure 3. Excitation and emission spectra of (a) LCSO:0.002Mn⁴⁺ and (b) LMSO:0.002Mn⁴⁺. Gaussian fitting of the energy-based excitation spectra (c) LCSO:0.002Mn⁴⁺ and (d) LMSO:0.002Mn⁴⁺. Emission spectra of (e) LCSO:0.002Mn⁴⁺ and (f) LMSO:0.002Mn⁴⁺ at 7 K.

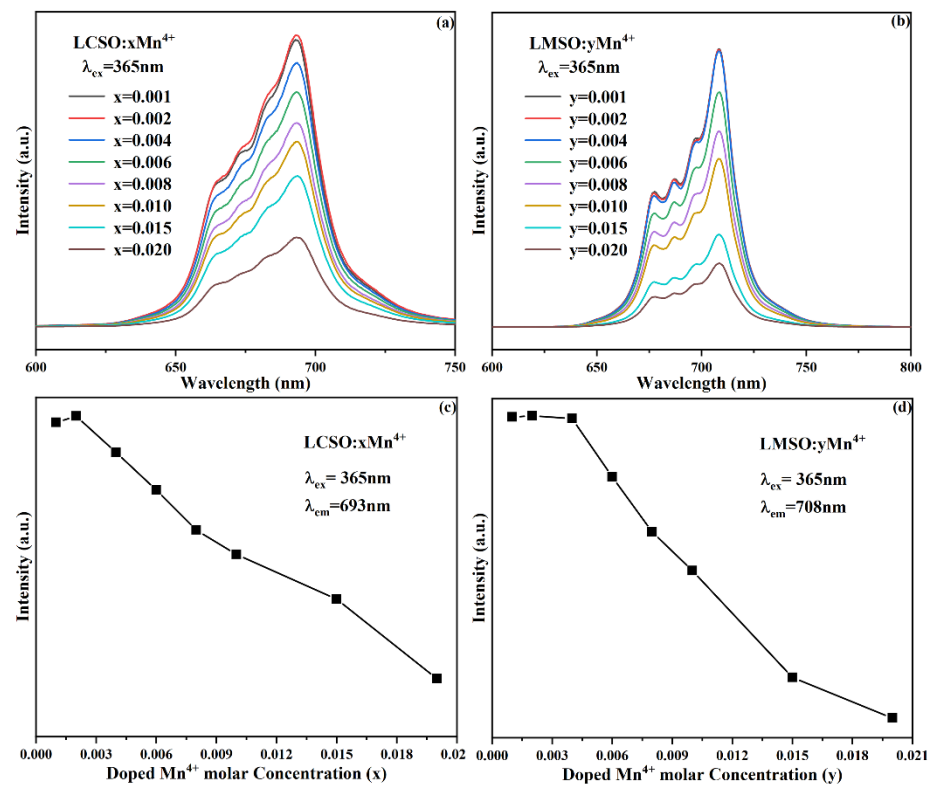


Figure 4. PL spectra of different amounts of Mn^{4+} in (a) LCSO and (b) LMSO under excitation at 365 nm. Relationship between doping concentration and emission intensity in (c) LCSO: $x\text{Mn}^{4+}$ and (d) LMSO: $y\text{Mn}^{4+}$.

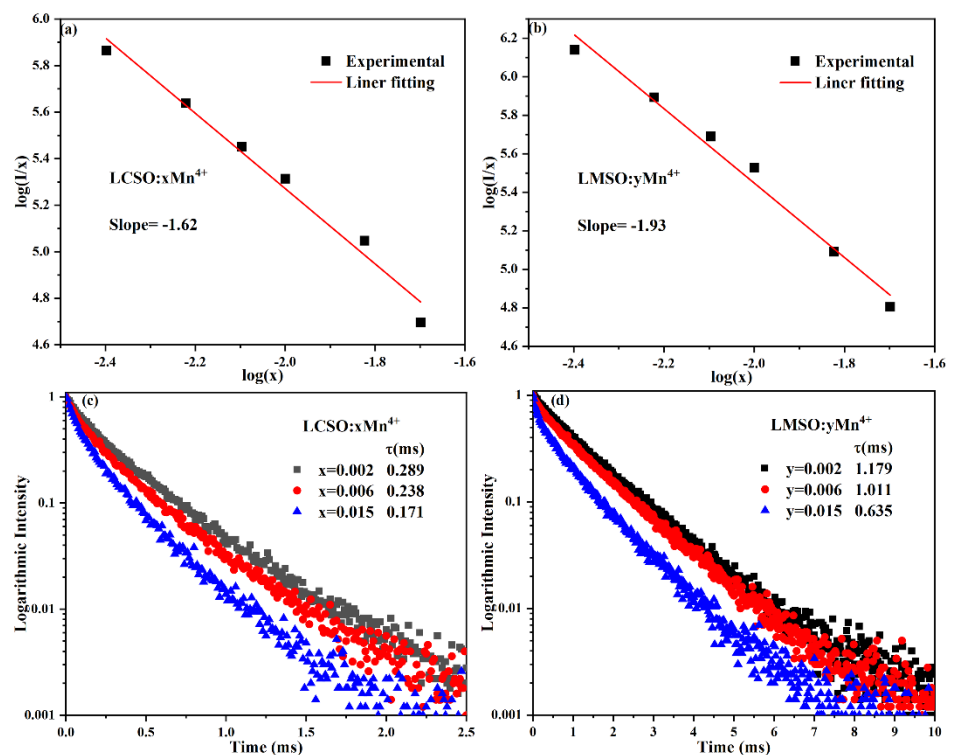


Figure 5. The linear fit of $\log(I/x)$ to $\log(x)$ of (a) LCSO: $x\text{Mn}^{4+}$ and (b) LMSO: $y\text{Mn}^{4+}$; fluorescence decay curves of (c) LCSO: $x\text{Mn}^{4+}$ and (d) LMSO: $y\text{Mn}^{4+}$.

Figure 5c,d present luminescence decay curves of LCSO: $x\text{Mn}^{4+}$ ($x = 0.002, 0.006, 0.015$) and LMSO: $y\text{Mn}^{4+}$ ($y = 0.002, 0.006, 0.015$). All decay curves can be described by fitting the effective decay time τ , which is calculated as [27]:

$$\tau = \frac{\int_0^{\infty} tI(t)dt}{\int_0^{\infty} I(t)dt} \quad (3)$$

where $I(t)$ means the luminescence intensity of Mn^{4+} at moment t . As the doping concentration of Mn^{4+} ions increases, the effective lifetimes were calculated to be 0.289, 0.238, and 0.171 ms for LCSO: $x\text{Mn}^{4+}$ ($x = 0.002, 0.006, 0.015$) and 1.179, 1.011, and 0.635 ms for LMSO: $y\text{Mn}^{4+}$ ($y = 0.002, 0.006, 0.015$), respectively. The decrease in the effective lifetimes is due to the increase in non-radiative energy transfer with the increase in Mn^{4+} doping concentration [28].

In addition, we tested the internal quantum yields (IQYs) of LCSO:0.002 Mn^{4+} and LMSO:0.002 Mn^{4+} , as shown in Figure 6. The IQYs were 22.90% for LCSO:0.002 Mn^{4+} and 35.48% for LMSO:0.002 Mn^{4+} under 365 nm excitation. The IQY of LMSO: 0.002 Mn^{4+} is higher than some previously reported Mn^{4+} -doped samples, as shown in Table 2.

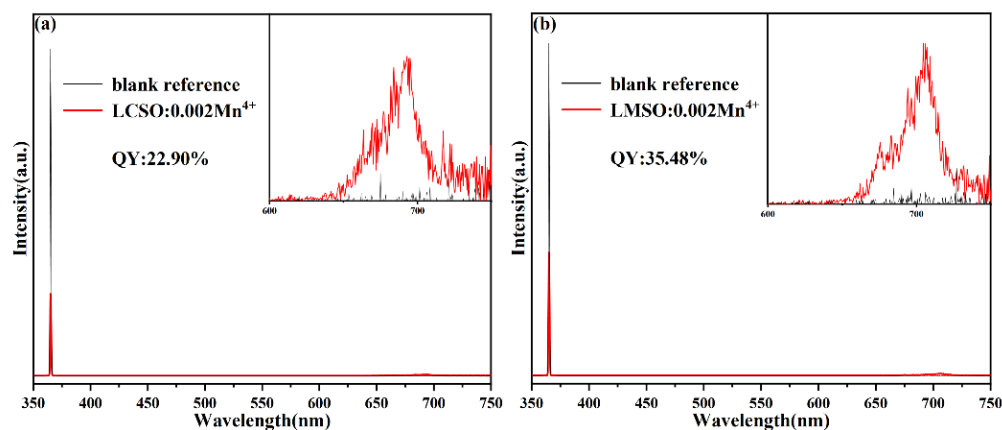


Figure 6. (a) IQY chart of LCSO:0.002 Mn^{4+} . (b) IQY chart of LMSO:0.002 Mn^{4+} .

Table 2. The luminescence properties of $\text{La}_2(\text{Ca}/\text{Mg})\text{SnO}_6:\text{Mn}^{4+}$ and other Mn^{4+} -doped phosphors.

Phosphor Composition	λ_{ex} (nm)	λ_{em} (nm)	IQY	References
$\text{Ba}_2\text{YNbO}_6:\text{Mn}^{4+}$	360	695	29.2	[17]
$\text{Ca}_2\text{YSbO}_6:\text{Mn}^{4+}$	470	680	19.72	[18]
$\text{SrLaGa}_3\text{O}_7:\text{Mn}^{4+}$	380	715	13.83	[21]
$\text{La}_2\text{MgTiO}_6:\text{Mn}^{4+}$	350	710	32.5	[29]
$\text{Li}_2\text{MgTiO}_4:\text{Mn}^{4+}$	460	676	32	[30]
$\text{Li}_2\text{MgZrO}_4:\text{Mn}^{4+}$	335	670	32.3	[31]
LCSO: Mn^{4+}	365	693	22.90	This work
LMSO: Mn^{4+}	365	708	35.48	This work

2.3. Crystal Field Analysis and Nephelauxetic Effect

In general, the Tanabe–Sugano energy level diagram can be used to explain the energy level splitting of the Mn^{4+} ions in a six-coordinate octahedral environment and its spectral properties, as shown in Figure 7a. When irradiated with an external light source, the electrons in the ground state ${}^4\text{A}_{2g}$ absorb energy and jump to excited states ${}^4\text{T}_{1g}$, ${}^4\text{T}_{2g}$, and ${}^2\text{T}_{2g}$, and then, through a non-radiative energy conversion process, to the lowest excited state ${}^2\text{E}_g$, and finally return to the ground state; the energy is expressed in the form of red light. In this process, the crystal field strength (D_q) strongly influences the energy level transition of the Mn^{4+} ions due to the unique $3d^3$ electron configuration of Mn^{4+} [32].

The crystal field strength is calculated from the energy difference of ${}^4A_{2g} \rightarrow {}^4T_{2g}$ by the following equation [33,34]:

$$D_q = \frac{E({}^4A_{2g} - {}^4T_{2g})}{10} \quad (4)$$

in addition, the Racah parameter B can be evaluated by the following equation [35]:

$$\frac{D_q}{B} = \frac{15(x - 8)}{x^2 - 10x} \quad (5)$$

the value of x can be calculated as follows [35]:

$$x = \frac{E({}^4A_{2g} - {}^4T_{1g}) - E({}^4A_{2g} - {}^4T_{2g})}{D_q} \quad (6)$$

the Racah parameter C can be acquired by the expression [35]:

$$\frac{E({}^2E_g - {}^4A_{2g})}{B} = \frac{3.05C}{B} + 7.9 - \frac{1.8B}{D_q} \quad (7)$$

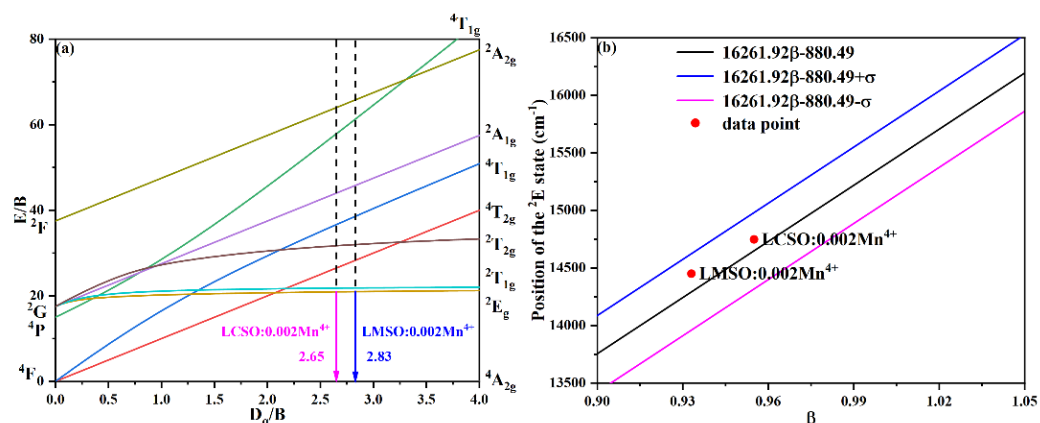


Figure 7. (a) Tanabe–Sugano diagram for Mn^{4+} (d^3) electron configuration in the octahedral site of LCSO and LMSO host. (b) Dependence of energy of the Mn^{4+} 2E_g level on the nephelauxetic ratio.

From the excitation spectrum and emission spectrum in Figure 3, the peak energies of the ${}^4A_{2g} \rightarrow {}^4T_{1g}$, ${}^4A_{2g} \rightarrow {}^4T_{2g}$, and ${}^2E_g \rightarrow {}^4A_{2g}$ are 25,943, 18,768, and 14,749 cm^{-1} for LCSO:0.002 Mn^{4+} and 26,381, 19,342, and 14,451 cm^{-1} for LMSO:0.002 Mn^{4+} , respectively. Substituting the above data into Equation (4)–(7), the values of D_q , B, C, and D_q/B were calculated to be 1876.8 cm^{-1} , 707.37 cm^{-1} , 3160.88 cm^{-1} , and 2.65 for LCSO:0.002 Mn^{4+} and 1934.2 cm^{-1} , 684.67 cm^{-1} , 3107.66 cm^{-1} , and 2.83 for LMSO:0.002 Mn^{4+} , respectively. The D_q/B values of both are greater than two and prove that the Mn^{4+} ions possess strong crystal fields in LCSO and LMSO hosts. In addition, the ${}^2E_g \rightarrow {}^4A_{2g}$ transition of the Mn^{4+} ions is hardly affected by the crystal field strength as shown by the Tanabe–Sugano energy level diagram. What can affect such a transition is a nephelauxetic effect that depends on the covalent relationship between the Mn^{4+} ions and the ligand [23,36–38]. Brik et al. introduced the nephelauxetic ratio (β) to describe the nephelauxetic effect, which was calculated as follows [34]:

$$\beta = \sqrt{\left(\frac{B}{B_0}\right)^2 + \left(\frac{C}{C_0}\right)^2} \quad (8)$$

where B_0 is 1160 cm^{-1} and C_0 is 4303 cm^{-1} represent the Racah parameters of Mn^{4+} -free ions. The β values of LCSO and LMSO were calculated as 0.955 and 0.933. On the basis

of previous experience with a large number of Mn^{4+} -doped crystals, a rule of thumb was established to predict the emission wavelength of Mn^{4+} with the following equation [32]:

$$E(^2E_g - ^4A_{2g}) = 16261.92\beta - 880.49 \pm \sigma \quad (9)$$

where σ is 332 cm^{-1} , a value close to the typical energy of phonon modes [12,32]. As shown in Figure 7b, the 2E_g energy levels calculated by this empirical formula are in the range $14,318\text{--}14,982 \text{ cm}^{-1}$ and $13,960\text{--}14,624 \text{ cm}^{-1}$ for LCSO:0.002Mn^{4+} and LMSO:0.002Mn^{4+} . The experimental values of the $^2E_g \rightarrow ^4A_{2g}$ transition are $14,430 \text{ cm}^{-1}$ for LCSO:0.002Mn^{4+} and $14,124 \text{ cm}^{-1}$ for LMSO:0.002Mn^{4+} , both of which are within the range.

2.4. Photoluminescence Thermal Stability

Figure 8a,b show the emission spectra of LCSO:0.002Mn^{4+} and LMSO:0.002Mn^{4+} with temperature under 365 nm excitation. The increase in temperature leads to an increase in lattice vibrations, which increases the nonradiative transition and produces a thermal quenching effect with a significant decrease in the intensity of the emission peak [39]. The poor thermal stability of both is due to the significant Stokes shift of Mn^{4+} ions in the crystal environment. In addition, the normalized emission intensity curves of the two samples (Figure 8c) indicate that the quenching temperatures ($T_{50\%}$) of the LCSO:0.002Mn^{4+} and LMSO:0.002Mn^{4+} samples are about 331 and 397 K, respectively. The LCSO:0.002Mn^{4+} phosphor exhibits a more serious decay trend between the two. To better understand the thermal quenching properties, the activation energy (E_a) is introduced to represent the energy difference between the cross-relaxation point and the excited state 2E_g , which can be calculated by the Arrhenius formula [40]:

$$\ln\left(\frac{I_0}{I} - 1\right) = \ln A - \frac{E_a}{kT} \quad (10)$$

where I_0 is the initial emission intensity, I is the emission intensity at temperature T , A is a constant, E_a is the activation energy, and k is the Boltzmann constant equal to $8.626 \times 10^{-5} \text{ eV/K}$. The specific linear relationship is described in Figure 9. E_a of LCSO:0.002Mn^{4+} is 0.38 eV, and E_a of LMSO:0.002Mn^{4+} is 0.40 eV. LCSO matrix structure is less stable than LMSO , resulting in lower activation energy and, thus, more prone to non-radiative processes, which eventually leads to a poor thermal stability. This situation is reflected in the configuration of the Mn^{4+} ions coordinate diagram (Figure 8d), indicating that smaller activation energy can excite the electron to reach the cross-relaxation point between the ground and excited states, followed by a radiation-free transition back to the ground state causing the quenching, thereby resulting in a lower quenching temperature [41].

2.5. Electroluminescence Spectrum of the Fabricated LED Devices

To demonstrate the potential application of these two red phosphors in plant growth, we prepared two far-red LED models with electroluminescence spectra and luminescence photographs, as shown in Figure 10a,b. The CIE coordinates of (0.6431, 0.3006) and (0.4948, 0.2909) for both under a voltage of 3.36 V and a current of 20 mA are shown in Figure 10d (numeral 1 and numeral 2), respectively. Both far-red LED devices emitted bright far-red light under 365 nm excitation, and their emission spectra matched well with the absorption spectra of plant photosensitive pigments Pr and Pfr.

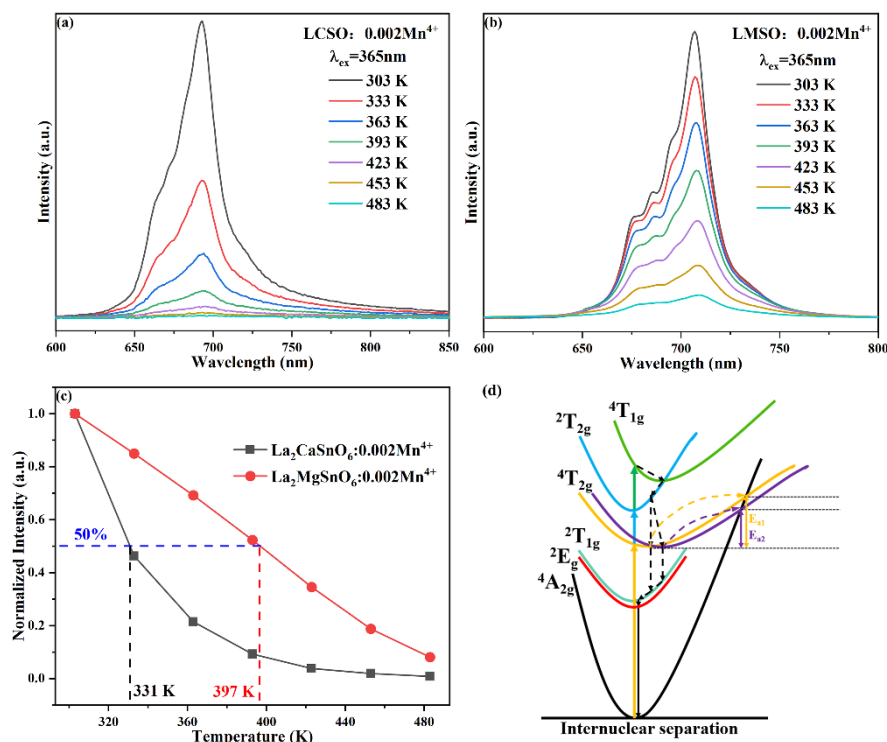


Figure 8. Emission intensity of (a) LCSO:0.002Mn⁴⁺ and (b) LMSO:0.002Mn⁴⁺ with temperature under 365 nm excitation. (c) Normalized intensity of the LCSO:0.002Mn⁴⁺ and LMSO:0.002Mn⁴⁺ as a function of temperature. (d) The configuration of the Mn⁴⁺ ions coordinate diagram.

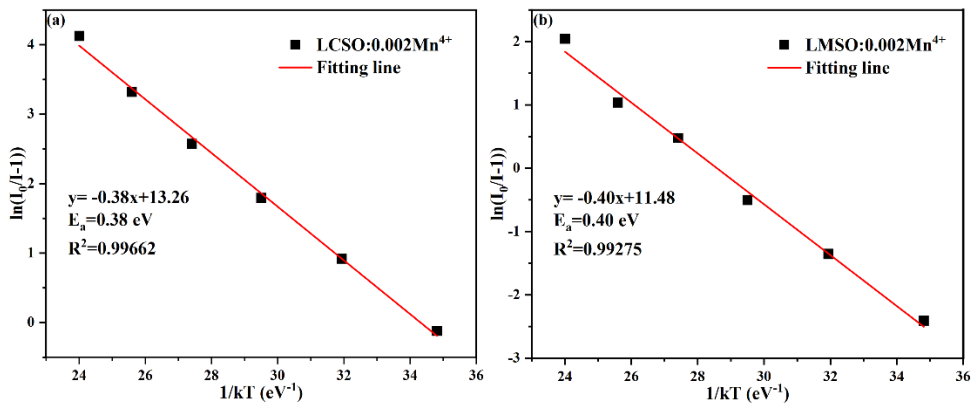


Figure 9. The linear relationship between $\ln(I_0/I)$ and $1/kT$ and the calculated activation energy (E_a) for LCSO: 0.002Mn⁴⁺ (a) and LMSO: 0.002Mn⁴⁺ (b).

In addition, to demonstrate the potential application of these two red phosphors in W-LEDs, three W-LED models were prepared, and their electroluminescence spectra, luminescence photographs, and performance parameters (color rendering index, correlated color temperature, and lumen efficiency) are shown in Figure 10c,e,f. The CIE coordinates of (0.3716, 0.4052), (0.3486, 0.3770), and (0.3386, 0.3648) for the three with a voltage of 3.36 V and a current of 20 mA are shown in Figure 10d (numeral 3, numeral 4, and numeral 5), respectively. Comparing Figure 10e,f with Figure 10c, we found that the addition of these two phosphors was able to overcome the problem of missing far-red light, and the color rendering index increased from 93 to 96.4 and 96.6. The above results indicate that LCSO:0.002Mn⁴⁺ and LMSO:0.002Mn⁴⁺ red phosphors can be used as candidates for W-LEDs.

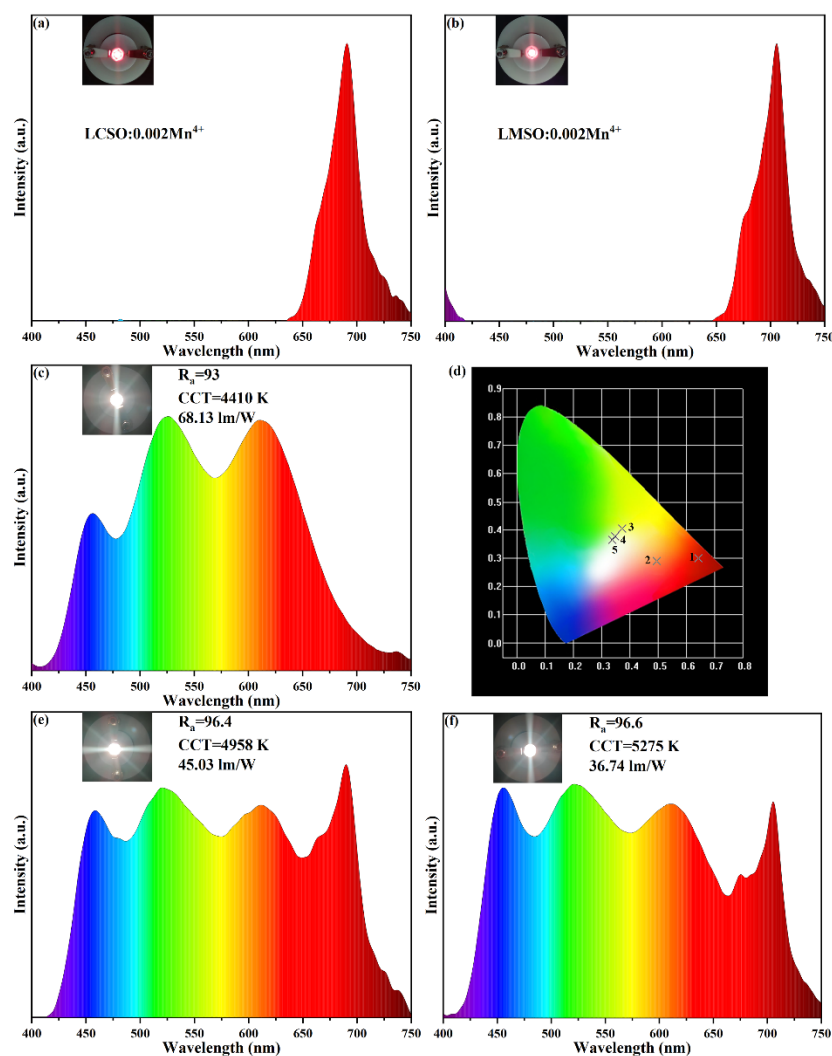


Figure 10. (a) Electroluminescence spectra of the LCSO:Mn⁴⁺. (b) Electroluminescence spectra of the LMSO:Mn⁴⁺. (c) Electroluminescence spectra of the BAM:Eu²⁺, (Sr,Ba)₂SiO₄:Eu²⁺, CaAlSiN₃:Eu²⁺. (d) The CIE chromaticity coordinate graph. (e) Electroluminescence spectra of the BAM:Eu²⁺, (Sr,Ba)₂SiO₄:Eu²⁺, CaAlSiN₃:Eu²⁺, and LCSO:Mn⁴⁺. (f) Electroluminescence spectra of the BAM:Eu²⁺, (Sr,Ba)₂SiO₄:Eu²⁺, CaAlSiN₃:Eu²⁺, and LMSO:Mn⁴⁺.

3. Materials and Methods

3.1. Sample Preparation

All La₂CaSn_{1-x}O₆:xMn⁴⁺ (abbreviated as LCSO:xMn⁴⁺, x = 0–0.01) and La₂MgSn_{1-y}O₆:yMn⁴⁺ (abbreviated as LMSO:yMn⁴⁺, y = 0–0.01) phosphors were synthesized by conventional high-temperature solid-state reaction. The raw materials were La₂O₃ (A.R.), CaCO₃ (A.R.), MgO (A.R.), SnO₂ (A.R.), and MnCO₃ (5N), which were weighed in the appropriate chemical proportions. After 20 minutes of thorough grinding in an agate mortar, the resulting mixture was transferred to an alumina crucible, warmed up at 4 °C per minute, preheated at 900 °C for 2 hours, and then sintered at 1480 °C for 3 hours in an air atmosphere. Finally, the samples were naturally cooled to room temperature and then reground into homogeneous powder for further measurements.

3.2. Characterization

The phase purity of the sintered samples was analyzed using powder X-ray diffraction (XRD) (AXS D8 Advance, Bruker, Karlsruhe, Germany) with graphite monochromatic Cu K α radiation ($\lambda = 0.15405$ nm) operating at 40 kV and 40 mA. Test from 10 to 80° in

steps of 0.02° with a counting time of 0.14s per step. XRD Rietveld refinement was performed using the Structural Analysis System (GSAS) program (Created by Brian H. Toby, Argonne Laboratories, USA). The X-ray photoelectron spectroscopy (XPS) data were obtained through a Thermo Scientific K-Alpha instrument (Thermo Fisher Scientific, Waltham, Massachusetts, USA) with a monochromatized Al K α line source, and the binding energy was calibrated to the C 1s peak at 284.8 eV. Photoluminescence emission (PL) and excitation (PLE) spectra were measured on a fluorescence spectrophotometer (F-7100, Hitachi, Tokyo, Japan) equipped with a 150 W xenon lamp. The luminescence decay curves and quantum yields (QY) were measured by an Edinburgh Instruments FLS-980 spectrometer (Edinburgh Instruments, Edinburgh, UK) equipped with an Edinburgh Instruments integrating sphere. The temperature-dependent photoluminescence emission (PL) spectra were tested on a phosphor excitation spectrum with thermal quenching analysis system EX-1000 (Hangzhou, China). The commercial blue phosphor BAM:Eu $^{2+}$, green phosphor (Sr,Ba) $_2$ SiO $_4$:Eu $^{2+}$, red phosphor CaAlSiN $_3$:Eu $^{2+}$, the as-synthesized La $_2$ (Ca,Mg)SnO $_6$:0.002Mn $^{4+}$, and UV-LED chips (365 nm) were used to fabricate W-LEDs. The luminescence characteristics of the white LED were evaluated using a Starspec SSP6612 (forward bias current, 20 mA, forward voltage, 3.36V) (Hangzhou, China).

4. Conclusions

In summary, a series of La $_2$ (Ca/Mg)SnO $_6$:Mn $^{4+}$ red phosphors were successfully prepared using a conventional high-temperature solid-state reaction. The Rietveld refinements revealed that both La $_2$ CaSnO $_6$:Mn $^{4+}$ and La $_2$ MgSnO $_6$:Mn $^{4+}$ were monoclinic phases and the Mn $^{4+}$ ions replace the Sn $^{4+}$ ions. The Tanabe–Sugano energy level diagrams indicate that the Mn $^{4+}$ ions were in a strong crystal field. In addition, LCSO:0.002Mn $^{4+}$ and LMSO:0.002Mn $^{4+}$ quantum yields were 22.90% and 35.48%, respectively. The thermal quenching phenomena of LCSO:0.002Mn $^{4+}$ and LMSO:0.002Mn $^{4+}$ were explained by the conformational coordinate diagram of the Mn $^{4+}$ ions. Finally, the obtained far-red LED devices emitted bright far-red light that matched well with the absorption spectra of plant photosensitive pigments Pr and Pfr. Additionally, the prepared W-LEDs had R $_a$ of 96.4 and 96.6 and CCT of 4958 K and 5275 K, respectively. These results show that LCSO:0.002Mn $^{4+}$ and LMSO:0.002Mn $^{4+}$ red phosphors can be used as the red component of W-LEDs as well as in plant growth.

Author Contributions: Investigation, J.W., H.Z. and L.W.; methodology, D.S.; data curation, Z.L. (Zheng Lu); formal analysis, Z.L. (Zeyu Lyu) and S.S.; writing—original draft, Z.L. (Zheng Lu); writing—review & editing, D.S. and H.Y. All authors have read and agreed to the published version of the manuscript.

Funding: This research was funded by the Research Projects of Ganjiang Innovation Academy, Chinese Academy of Sciences (E255C001), the National Natural Science Foundation of China (Grant Nos. 52072363), and the Key Research Program of the Chinese Academy of Sciences (Grant No. ZDRW-CN-2021-3-3).

Conflicts of Interest: The authors declare no conflict of interest.

References

1. Zhu, D.; Li, J.; Guo, X.; Li, Q.; Wu, H.; Meng, L.; Liu, Z. Controlled Synthesis of Tb $^{3+}$ /Eu $^{3+}$ Co-doped Gd $_2$ O $_3$ phosphors with enhanced red emission. *Molecules* **2019**, *24*, 759. [[CrossRef](#)] [[PubMed](#)]
2. Dai, P.P.; Li, C.; Zhang, X.T.; Xu, J.; Chen, X.; Wang, X.L.; Jia, Y.; Wang, X.; Liu, Y.C. A single Eu $^{2+}$ -activated high-color-rendering oxychloride white-light phosphor for white-light-emitting diodes. *Light Sci. Appl.* **2016**, *5*, e16024. [[CrossRef](#)] [[PubMed](#)]
3. Wang, Q.; Xie, M.; Fang, M.; Wu, X.; Liu, Y.; Huang, Z.; Xi, K.; Min, X. Synthesis and luminescence properties of a novel green-yellow-emitting phosphor BiOCl:Pr $^{3+}$ for Blue-Light-Based w-LEDs. *Molecules* **2019**, *24*, 1296. [[CrossRef](#)] [[PubMed](#)]
4. Zhang, W.; He, C.; Wu, X.; Huang, X.; Lin, F.; Liu, Y.; Fang, M.; Min, X.; Huang, Z. Yellow emission obtained by combination of broadband emission and multi-peak emission in garnet structure Na $_2$ YMg $_2$ V $_3$ O $_{12}$:Dy $^{3+}$ phosphor. *Molecules* **2020**, *25*, 542. [[CrossRef](#)] [[PubMed](#)]
5. Adachi, S. Review—Tanabe–Sugano energy-level diagram and Racah parameters in Mn $^{4+}$ -activated red and deep red-emitting phosphors. *ECS J. Solid State Sci. Technol.* **2019**, *8*, R183–R196. [[CrossRef](#)]

6. Zhou, C.; Peng, L.; Kong, Z.; Wu, M.; Molokeev, M.S.; Zhou, Z.; Wang, J.; Xia, M. A high thermal stability Cr³⁺-doped gallate far red phosphor for plant lighting: Structure, luminescence enhancement and application prospect. *J. Mater. Chem. C* **2022**, *10*, 5829–5839. [[CrossRef](#)]
7. Zhang, L.; Xu, Y.; Yin, S.; You, H. Rare-earth-free Mn⁴⁺-doped double perovskite structure phosphor for near ultraviolet excitation of WLED and plant cultivation. *J. Alloys Compd.* **2022**, *891*, 162042. [[CrossRef](#)]
8. Zhang, H.; Zhang, J.; Su, Y.; Zhang, X. Metal to metal charge transfer induced efficient yellow/far-red luminescence in Na₂Ca₃(Nb,Ta)₂O₉:Bi³⁺ toward the applications of white-LEDs and plant growth light. *Adv. Opt. Mater.* **2022**, *10*, 2200150. [[CrossRef](#)]
9. Zhou, Y.; Yu, C.; Song, E.; Wang, Y.; Ming, H.; Xia, Z.; Zhang, Q. Three birds with one stone: K₂SiF₆:Mn⁴⁺ single crystal phosphors for high-power and laser-driven lighting. *Adv. Opt. Mater.* **2020**, *8*, 2000976. [[CrossRef](#)]
10. Wu, Y.; Zhuang, Y.; Lv, Y.; Ruan, K.; Xie, R.-J. A high-performance non-rare-earth deep-red-emitting Ca_{14-x}Sr_xZn₆Al₁₀O₃₅:Mn⁴⁺ phosphor for high-power plant growth LEDs. *J. Alloys Compd.* **2019**, *781*, 702–709. [[CrossRef](#)]
11. Deng, K.; Jin, Y.; Yuan, L.; Wang, B.; Wu, H.; Hu, Y. A thermal-stable Mn⁴⁺-doped far-red-emitting phosphor-converted LED for indoor plant cultivation. *Mater. Today Chem.* **2022**, *26*, 101010. [[CrossRef](#)]
12. Wang, Z.; Lin, H.; Zhang, D.; Shen, Y.; Li, Y.; Hong, R.; Tao, C.; Han, Z.; Chen, L.; Zhou, S. Deep-red emitting Mg₂TiO₄:Mn⁴⁺ phosphor ceramics for plant lighting. *J. Adv. Ceram.* **2020**, *10*, 88–97. [[CrossRef](#)]
13. Li, L.; Tian, G.; Chang, W.; Yan, Y.; Ling, F.; Jiang, S.; Xiang, G.; Zhou, X. A novel double-perovskite LiLaMgTeO₆:Mn⁴⁺ far-red phosphor for indoor plant cultivation white LEDs: Crystal and electronic structure, and photoluminescence properties. *J. Alloys Compd.* **2020**, *832*, 154905. [[CrossRef](#)]
14. Gu, S.; Xia, M.; Zhou, C.; Kong, Z.; Molokeev, M.S.; Liu, L.; Wong, W.-Y.; Zhou, Z. Red shift properties, crystal field theory and nephelauxetic effect on Mn⁴⁺-doped SrMgAl_{10-y}Ga_yO₁₇ red phosphor for plant growth LED light. *Chem. Eng. J.* **2020**, *396*, 125208. [[CrossRef](#)]
15. Xu, Y.; Zhang, L.; Dong, L.; Yin, S.; Wu, X.; You, H. Novel SrGd₂Al₂O₇:Mn⁴⁺, Nd³⁺, and Yb³⁺ phosphors for c-Si solar cells. *Dalton Trans.* **2021**, *50*, 7017–7025. [[CrossRef](#)]
16. Qin, L.; Bi, S.; Cai, P.; Chen, C.; Wang, J.; Kim, S.I.; Huang, Y.; Seo, H.J. Preparation, characterization and luminescent properties of red-emitting phosphor: LiLa₂NbO₆ doped with Mn⁴⁺ ions. *J. Alloys Compd.* **2018**, *755*, 61–66. [[CrossRef](#)]
17. Fu, A.; Pang, Q.; Yang, H.; Zhou, L. Ba₂YNbO₆:Mn⁴⁺-based red phosphor for warm white light-emitting diodes (WLEDs): Photoluminescent and thermal characteristics. *Opt. Mater.* **2017**, *70*, 144–152. [[CrossRef](#)]
18. Zhong, J.; Chen, D.; Chen, X.; Wang, K.; Li, X.; Zhu, Y.; Ji, Z. Efficient rare-earth free red-emitting Ca₂YSbO₆:Mn⁴⁺, M(M = Li⁺, Na⁺, K⁺, Mg²⁺) phosphors for white light-emitting diodes. *Dalton Trans.* **2018**, *47*, 6528–6537. [[CrossRef](#)]
19. Cao, R.; Chen, T.; Ren, Y.; Chen, T.; Ao, H.; Li, W.; Zheng, G. Synthesis and photoluminescence properties of Ca₂LaTaO₆:Mn⁴⁺ phosphor for plant growth LEDs. *J. Alloys Compd.* **2019**, *780*, 749–755. [[CrossRef](#)]
20. Wu, Q.; Li, P.; Ye, Z.; Huo, X.; Yang, H.; Wang, Y.; Wang, D.; Zhao, J.; Yang, Z.; Wang, Z. Near-infrared emitting phosphor LaMg_{0.5}SnGe_{0.5}O₃:Cr³⁺ for plant growth applications: Crystal structure, luminescence, and thermal stability. *Inorg. Chem.* **2021**, *60*, 16593–16603. [[CrossRef](#)]
21. Gai, S.; Zhu, H.; Gao, P.; Zhou, C.; Kong, Z.; Molokeev, M.S.; Qi, Z.; Zhou, Z.; Xia, M. Structure analysis, tuning photoluminescence and enhancing thermal stability on Mn⁴⁺-doped La_{2-x}Y_xMgTiO₆ red phosphor for agricultural lighting. *Ceram. Int.* **2020**, *46*, 20173–20182. [[CrossRef](#)]
22. Zheng, Y.; Zhang, H.; Zhang, H.; Xia, Z.; Liu, Y.; Molokeev, M.S.; Lei, B. Co-substitution in Ca_{1-x}Y_xAl_{12-x}Mg_xO₁₉ phosphors: Local structure evolution, photoluminescence tuning and application for plant growth LEDs. *J. Mater. Chem. C* **2018**, *6*, 4217–4224. [[CrossRef](#)]
23. Chen, H.; Lin, H.; Huang, Q.; Huang, F.; Xu, J.; Wang, B.; Lin, Z.; Zhou, J.; Wang, Y. A novel double-perovskite Gd₂ZnTiO₆:Mn⁴⁺ red phosphor for UV-based w-LEDs: Structure and luminescence properties. *J. Mater. Chem. C* **2016**, *4*, 2374–2381. [[CrossRef](#)]
24. Blasse, G. Energy transfer in oxidic phosphors. *Phys. Lett. A* **1968**, *28*, 444–445. [[CrossRef](#)]
25. Dong, L.; Zhang, L.; Lu, W.; Shao, B.; Zhao, S.; You, H. Preparation and photoluminescence of novel La₈Ca₂(Si₄P₂O₂₂N₂)O₂ oxynitride phosphors containing Eu²⁺/Ce³⁺/Tb³⁺ ions. *Dalton Trans.* **2019**, *48*, 3028–3037. [[CrossRef](#)]
26. Wu, D.; Xiao, Y.; Zhang, L.; Dong, X.; Zhao, S.; Zhou, W.; Lu, Q.; Zhang, J. Highly efficient and thermally stable luminescence of Ca₃Gd₂Si₆O₁₈:Ce³⁺,Tb³⁺ phosphors based on efficient energy transfer. *J. Mater. Chem. C* **2020**, *8*, 17176–17184. [[CrossRef](#)]
27. Shao, B.; Huo, J.; You, H. Prevailing strategies to tune emission color of lanthanide-activated phosphors for WLED applications. *Adv. Opt. Mater.* **2019**, *7*, 1900319. [[CrossRef](#)]
28. Zhu, M.; Pan, Y.; Huang, Y.; Lian, H.; Lin, J. Designed synthesis, morphology evolution and enhanced photoluminescence of a highly efficient red dodec-fluoride phosphor, Li₃Na₃Ga₂F₁₂:Mn⁴⁺, for warm WLEDs. *J. Mater. Chem. C* **2018**, *6*, 491–499. [[CrossRef](#)]
29. Yuan, H.; Huang, Z.; Xu, L.; Jia, H.; Sun, X.; Liu, K. La₂MgTiO₆:Bi³⁺/Mn⁴⁺ photoluminescence materials: Molten salt preparation, Bi³⁺ → Mn⁴⁺ energy transfer and thermostability. *J. Lumin.* **2020**, *224*, 117290. [[CrossRef](#)]
30. Xing, G.; Feng, Y.; Pan, M.; Wei, Y.; Li, G.; Dang, P.; Liang, S.; Molokeev, M.S.; Cheng, Z.; Lin, J. Photoluminescence tuning in a novel Bi³⁺/Mn⁴⁺ co-doped La₂ATiO₆(A = Mg, Zn) double perovskite structure: Phase transition and energy transfer. *J. Mater. Chem. C* **2018**, *6*, 13136–13147. [[CrossRef](#)]

31. Cao, R.; Shi, Z.; Quan, G.; Chen, T.; Guo, S.; Hu, Z.; Liu, P. Preparation and luminescence properties of $\text{Li}_2\text{MgZrO}_4:\text{Mn}^{4+}$ red phosphor for plant growth. *J. Lumin.* **2017**, *188*, 577–581. [[CrossRef](#)]
32. Brik, M.G.; Camardello, S.J.; Srivastava, A.M. Influence of covalency on the $\text{Mn}^{4+} {}^2\text{E}_g \rightarrow {}^4\text{A}_{2g}$ emission energy in crystals. *ECS J. Solid State Sci. Technol.* **2014**, *4*, R39–R43. [[CrossRef](#)]
33. Reisfeld, M.J.; Matwiyoff, N.A.; Asprey, L.B. The electronic spectrum of cesium hexafluoromanganese(IV). *J. Mol. Spectrosc.* **1971**, *39*, 8–20. [[CrossRef](#)]
34. Brik, M.G.; Srivastava, A.M. Electronic energy levels of the Mn^{4+} ion in the Perovskite, CaZrO_3 . *ECS J. Solid State Sci. Technol.* **2013**, *2*, R148–R152. [[CrossRef](#)]
35. Zhou, Z.; Zheng, J.; Shi, R.; Zhang, N.; Chen, J.; Zhang, R.; Suo, H.; Goldys, E.M.; Guo, C. Ab initio site occupancy and far-red emission of Mn^{4+} in cubic-phase $\text{La}(\text{MgTi})_{1/2}\text{O}_3$ for plant cultivation. *ACS Appl. Mater. Inter.* **2017**, *9*, 6177–6185. [[CrossRef](#)]
36. Zhang, X.; Nie, J.; Liu, S.; Li, Y.; Qiu, J. Deep-red photoluminescence and long persistent luminescence in double perovskite-type $\text{La}_2\text{MgGeO}_6:\text{Mn}^{4+}$. *J. Am. Ceram. Soc.* **2018**, *101*, 1576–1584. [[CrossRef](#)]
37. Jin, Y.; Hu, Y.; Wu, H.; Duan, H.; Chen, L.; Fu, Y.; Ju, G.; Mu, Z.; He, M. A deep red phosphor $\text{Li}_2\text{MgTiO}_4:\text{Mn}^{4+}$ exhibiting abnormal emission: Potential application as color converter for warm w-LEDs. *Chem. Eng. J.* **2016**, *288*, 596–607. [[CrossRef](#)]
38. Srivastava, A.M.; Beers, W.W. Luminescence of Mn^{4+} in the distorted Perovskite $\text{Gd}_2\text{MgTiO}_6$. *J. Electrochem. Soc.* **2019**, *143*, L203–L205. [[CrossRef](#)]
39. Liu, Y.; Zhou, Z.; Huang, L.; Brik, M.G.; Si, S.; Lin, L.; Xuan, T.; Liang, H.; Qiu, J.; Wang, J. High-performance and moisture-resistant red-emitting $\text{Cs}_2\text{SiF}_6:\text{Mn}^{4+}$ for high-brightness LED backlighting. *J. Mater. Chem. C* **2019**, *7*, 2401–2407. [[CrossRef](#)]
40. Dong, L.; Zhang, L.; Jia, Y.; Shao, B.; Lu, W.; Zhao, S.; You, H. Enhancing luminescence and controlling the Mn valence state of $\text{Gd}_3\text{Ga}_{5-x}\text{Al}_x\text{O}_{12}:\text{yMn}$ phosphors by the design of the garnet structure. *ACS Appl. Mater. Inter.* **2020**, *12*, 7334–7344.
41. Li, L.; Chang, W.; Chen, W.; Feng, Z.; Zhao, C.; Jiang, P.; Wang, Y.; Zhou, X.; Suchocki, A. Double perovskite $\text{LiLaMgWO}_6:\text{Eu}^{3+}$ novel red-emitting phosphors for solid state lighting: Synthesis, structure and photoluminescent properties. *Ceram. Int.* **2017**, *43*, 2720–2729. [[CrossRef](#)]